Collisional microwave heating and wall interaction of an ultracold plasma in a resonant microwave cavity

PAPER • OPEN ACCESS

Collisional microwave heating and wall interaction of an ultracold plasma in a resonant microwave cavity

New Journal of Physics
The open access journal at the forefront of physics

Deutsche Physikalische Gesellschaft DPG
IOP Institute of Physics

Published in partnership with: Deutsche Physikalische Gesellschaft and the Institute of Physics

OPEN ACCESS

RECEIVED
15 December 2021

REVISED
13 April 2022

ACCEPTED FOR PUBLICATION
3 May 2022

PUBLISHED
17 June 2022

PAPER

Collisional microwave heating and wall interaction of an ultracold plasma in a resonant microwave cavity

M A W van Ninhuijs[1], J Beckers[2] and O J Luiten[1,*]

[1] Department of Applied Physics, Coherence and Quantum Technology Group, Eindhoven University of Technology, PO Box 513, 5600 MB Eindhoven, The Netherlands
[2] Department of Applied Physics, Elementary Processes in Gas Discharges Group, Eindhoven University of Technology, PO Box 513, 5600 MB Eindhoven, The Netherlands
[*] Author to whom any correspondence should be addressed.

E-mail: o.j.luiten@tue.nl

Keywords: ultracold plasma, collisional microwave heating, plasma–wall interaction model, microwave cavity resonance spectroscopy

Abstract

Recently, we introduced a resonant microwave cavity as a diagnostic tool for the study of ultracold plasmas (UCPs). This diagnostic allows us to study the electron dynamics of UCPs non-destructively, very fast, and with high sensitivity by measuring the shift in the resonance frequency of a cavity, induced by a plasma. However, in an attempt to theoretically predict the frequency shift using a Gaussian self-similar expansion model, a three times faster plasma decay was observed in the experiment than found in the model. For this, we proposed two causes: plasma–wall interactions and collisional microwave heating. In this paper, we investigate the effect of both causes on the lifetime of the plasma. We present a simple analytical model to account for electrons being lost to the cavity walls. We find that the model agrees well with measurements performed on plasmas with different initial electron temperatures and that the earlier discrepancy can be attributed to electrons being lost to the walls. In addition, we perform measurements for different electric field strengths in the cavity and find that the electric field has a small, but noticeable effect on the lifetime of the plasma. By extending the model with the theory of collisional microwave heating, we find that this effect can be predicted quite well by treating the energy transferred from the microwave field to the plasma as additional initial excess energy for the electrons.

1. Introduction

With typical particle number densities of 10^{16} m^{-3}, and temperatures as low as $\sim$1 K for electrons and a few hundreds of microkelvins for ions, ultracold plasmas (UCPs) form a new exotic category of plasmas in which the limits of conventional theories in plasma physics can be tested experimentally [1].

UCPs can be produced from ultracold atoms in a magneto-optical trap (MOT) by photo-ionizing the atoms just above their ionization threshold [2]; the amount of excess energy of the ionization laser's photons, and the laser's intensity profile determine the initial temperature of the electrons, and the plasma density distribution, respectively. This makes it possible to create a plasma with much better controlled initial conditions than in many other more conventional plasmas [3].

One of the remarkable features of UCPs is that they can also get strongly coupled, a condition in which the average thermal energy between the particles in the plasma is less than their electrostatic potential energy. As a result, correlations between particles become important, and kinetic plasma theory, which assumes a large number of particles within a Debye sphere to screen the long-range Coulomb interactions, breaks down. This condition is quantified by the so-called coupling parameter $\Gamma_\alpha > 1$, with Γ_α being defined as

$$\Gamma_\alpha \equiv \frac{q_\alpha^2}{4\pi\epsilon_0 a k_B T_\alpha}. \tag{1}$$

Here, ϵ_0 is the vacuum permittivity, a the Wigner–Seitz radius, k_B the Boltzmann constant, and q_α and T_α the charge and temperature of the particle species α, respectively ($\alpha =$ e for electrons and $\alpha =$ i for ions).

Experimentally, strong coupling can be observed in complex plasmas [4–6] and ionic plasmas, where it may lead to Wigner crystallization. Similar conditions that may result in strong coupling are expected to be found in astrophysical systems, such as white dwarfs, Jovian planets, and the crust of neutron stars [7, 8].

However, in the case of UCPs, certain heating mechanisms such as three-body recombination for the electrons (due to the strong $T_e^{-9/2}$ rate dependence [9]), and disorder-induced heating for both electrons [10] and ions [11] are preventing the plasma to go into the strongly coupled regime. Only recently, Killian *et al* managed to obtain an ionic coupling parameter as high as 11, by laser cooling the ions in a Sr UCP [12].

UCPs are typically studied with techniques which are employed in the field of atomic and particle physics as well: charged particle diagnostics and optical techniques, such as laser-induced fluorescence [13] and absorption imaging [14]. Charged particle detection, on the one hand, uses a static electric field to capture the density profile of either the electrons or ions in the plasma by accelerating them to a nearby microchannel plate detector with a static electric field. This technique allows the dynamics of the plasma profile to be monitored at microsecond timescales, but is destructive for the plasma as a whole [1]. The optical techniques, on the other hand, make it possible to capture the dynamics of the ions in a UCP non-destructively and with a much higher temporal resolution, but are limited to UCPs with ions that possess ground state electric-dipole-allowed transitions accessible to lasers and cameras [15]; they are therefore not applicable to UCPs of all atomic species.

Recently, we introduced a new type of diagnostic for the study of UCPs that combines some of the advantages provided by previous UCP diagnostic techniques; it allows the plasma to be followed simultaneously in a non-destructive manner, with nanosecond temporal resolution, high sensitivity, and is, as a technique, applicable to UCPs of all atomic species [16, 17].

This diagnostic tool is a 5 GHz microwave cavity with a compact diffraction grating-based magneto-optical trap inside to laser cool and trap a cloud of ^{85}Rb atoms [18, 19]. It uses the shift in the resonance frequency of the cavity, induced by the UCP created from this ultracold atomic cloud, to retrieve information on the electron dynamics of the plasma. The technique of using the frequency shift of a cavity to probe a plasma is known as *microwave cavity resonance spectroscopy* (MCRS) [20–22] and has been used before to study the dynamics of some other types of plasmas, such as low-pressure rf plasmas [23], etching plasmas [24, 25], powder-forming plasmas [26], and more recently, plasmas induced by extreme ultraviolet irradiation [27] and atmospheric-pressure plasma jets [28–30].

Although MCRS is an established method to measure the electron dynamics of plasmas, for UCPs, a full quantitative comparison of the measured MCRS signal with a theoretical model has not been given so far. In a first attempt to theoretically predict the MCRS signal in the study of an ultracold ^{85}Rb plasma with the aforementioned cavity, we found a quite good agreement between the measured shift in the resonance frequency of the cavity, immediately after photo-ionization of the atomic cloud, and the theoretically predicted shift, based on the knowledge of the atomic cloud, the laser beams used, and the photo-ionization cross section of rubidium. However, we also observed that the plasma decayed three times faster than predicted by a self-similar Gaussian expansion model [31]. We proposed two potential explanations for the increased plasma decay: collisional microwave heating or inverse Bremsstrahlung, in which electrons quivering in the Coulomb fields of the stationary ions deflect and absorb part of the cavity's microwave energy [32], and plasma–wall absorption.

In this paper, we investigate both decay mechanisms. We performed measurements of the plasma decay with MCRS for different rf electric field strengths in the cavity. In addition, we developed an analytical microscopic plasma model, derived from the macroscopic Gaussian self-similar expansion model, to predict the flux and thus the loss of electrons to the cavity walls. We validated this model with MCRS measurements performed on UCPs with different initial electron temperatures. We will show that the cavity's electric field indeed influences the lifetime of the plasma, but that this effect is rather subtle; we will demonstrate that the major cause for the observed increase in plasma decay can be attributed to losses of electrons from the plasma to the cavity walls, which is described quite well by the analytical plasma model. In addition, by extending the model with the theory of collisional microwave heating, we find that the measurements performed on plasmas with different rf electric field strengths in the cavity can be predicted quite well by treating the energy transferred from the microwave field to the plasma as additional initial excess energy for the electrons.

This paper is organized as follows. In section 2, the experimental setup is described and the technique of MCRS is discussed in more detail. Then, in section 3, the measurements of the effect of the cavity's rf electric field on the decay time of the plasma are presented. Subsequently, the plasma model is discussed (section 4); from the macroscopic self-similar expansion model, discussed in section 4.1, we derive the equations for the microscopic model, which are presented in section 4.2. To verify the microscopic model, we perform MCRS measurements on UCPs with different initial electron temperatures (section 4.3), and

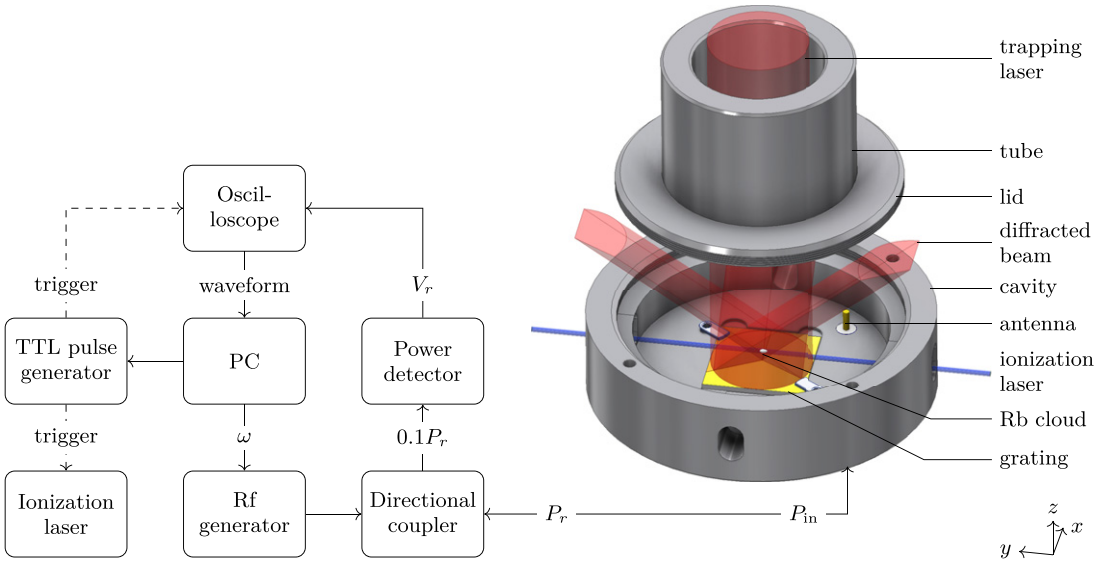

Figure 1. Experimental setup with the microwave cavity and a schematic representation of the data-acquisition system used to measure the frequency shift of the cavity induced by a UCP.

subsequently, in section 4.4, the limitations of the microscopic model are discussed. To explain the rf electric field measurements presented in section 3, the microscopic model is extended in section 5, by including the theory of collisional microwave heating, and the model is subsequently compared to the rf electric field measurements. Finally, in section 6, the conclusions and outlook are presented.

2. Experiment and methods

To produce a UCP and to perform MCRS experiments, we make use of the setup depicted in figure 1, and follow similar steps as described in reference [17].

We laser cool and trap ^{85}Rb atoms in the overlap volume formed by the incident and diffracted trapping laser beams above a diffraction grating chip [18, 19] inside a 5 GHz microwave cavity.

Next, we use a two-step photo-ionization scheme to create a UCP; we excite the atoms from the $5^2S_{1/2}(F = 3)$ ground state to the $5^2P_{3/2}(F^{'} = 4)$ excited state with the 780 nm trapping laser as excitation laser, and subsequently we photo-ionize the atoms just above their ionization threshold using a tunable 480 nm pulsed dye laser (6 ns). This laser enters the cavity through one of the access holes, and its wavelength is set to 477.867 nm, 476.679 nm, 474.322 nm, and 467.388 nm to create plasmas with initial electron temperatures of 50 K, 100 K, 200 K, and 500 K, respectively.

Once the plasma is created, we measure the shift in the resonance frequency of the cavity, induced by the presence of the plasma, with the data-acquisition system depicted in figure 1. We perform a frequency scan with an rf generator controlled by a pc, for frequencies $\omega/2\pi$ ranging from 4948 MHz to 4958 MHz, in steps of 100 kHz. The output power of the rf generator depends on the experiment, and is set between -20 dBm and 10 dBm. For each applied frequency ω in a scan, we electrically couple an amount of rf power P_{in} to the 5 GHz TM_{010} eigenmode of the cavity with a linear antenna, and measure (ten percent of) the reflected power P_{r} with a power detector behind a directional coupler. The detector converts the measured power into a voltage V_{r}, which is recorded as a function of time with an oscilloscope, as illustrated in figure 2 by some waveforms that were acquired for different applied frequencies to the cavity near its unperturbed resonance frequency $\omega_0/2\pi \approx 4952.95$ MHz. The waveforms can be used to reconstruct a set of Lorentzian curves describing the cavity's resonant behavior for each time step. From these curves, the frequency shift $\Delta\omega(t)$ as a function of time t can be determined.

For a collisionless nonmagnetized UCP, the resonance frequency shift is related to the electron density by [33]

$$\frac{\Delta\omega(t)}{\omega_0} = \frac{e^2}{2m_{\text{e}}\epsilon_0\omega_0^2}\overline{n}_{\text{e}}(t), \tag{2}$$

with e the elementary charge, m_{e} the electron mass, ω_0 the resonance frequency of the empty (vacuum) cavity, and $\overline{n}_{\text{e}}(t)$ the so-called field-averaged electron density. The field-averaged electron density is defined as

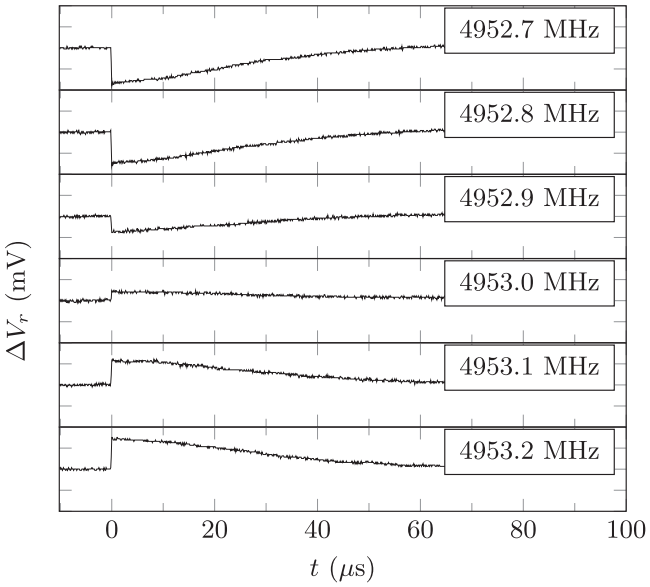

Figure 2. The change in the cavity reflection voltage $\Delta V_\mathrm{r} \equiv V_\mathrm{r} - V_0$ as a function of time t for six different applied frequencies $\omega/2\pi$ to the cavity, due to the creation of a UCP at $t = 0$, with V_0 being the average reflection voltage for $t < 0$.

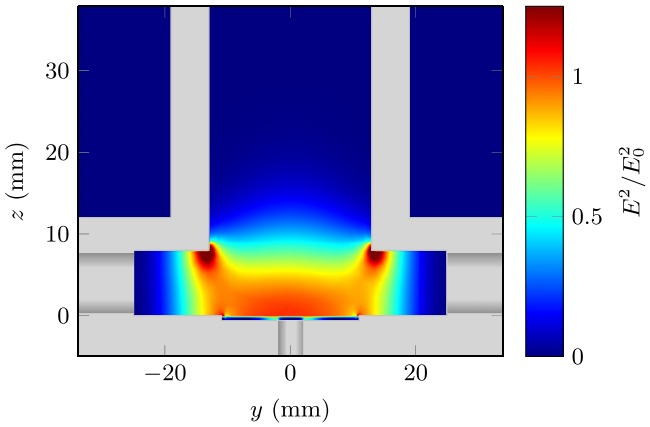

Figure 3. The simulated electric field profile of the TM_{010} mode of the cavity, at different positions in the yz-plane. The color indicates the square of the normalized electric field amplitude E/E_0, with E_0 being the field amplitude at position $x = 0$ mm, $y = 0$ mm, and $z = 2$ mm. Reproduced from [17]. CC BY 4.0.

$$\overline{n}_\mathrm{e}(t) \equiv \frac{\int_{V_\mathrm{cav}} n_\mathrm{e}(\mathbf{r},t)|\mathbf{E}(\mathbf{r})|^2 \mathrm{d}^3\mathbf{r}}{\int_{V_\mathrm{cav}} |\mathbf{E}(\mathbf{r})|^2 \mathrm{d}^3\mathbf{r}}, \tag{3}$$

and represents the weighted average of the local electron density n_e in the plasma, with the square of the electric field $\mathbf{E}$ of the used resonant eigenmode of the cavity as a weight factor; it is calculated over all positions $\mathbf{r}$ in the cavity volume V_cav, with $\mathbf{r} \equiv (x, y, z)^\mathrm{T}$ being a position in Cartesian coordinates with respect to the center of the diffraction grating chip in the cavity.

To interpret measurements of the decay of the field-averaged electron density $\overline{n}_\mathrm{e}(t)$ in terms of plasma dynamics, an electric field map of the used eigenmode of the cavity, and a plasma model describing the electron dynamics as a function of position and time are needed.

In section 4.2, a plasma model is presented. For the electric field, we use the field-map of the simulated TM_{010} mode of the cavity, see figure 3. This field-map was previously obtained from simulations performed in CST Microwave Studio [34] and verified with bead-pull measurements of the electric field (see reference [17]).

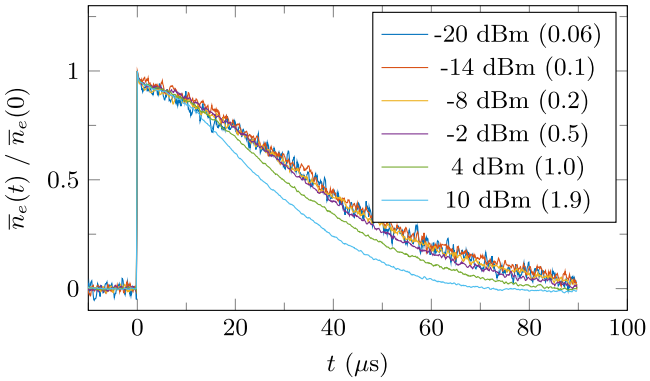

Figure 4. The normalized field-averaged electron density $\overline{n}_e(t)/\overline{n}_e(0)$ as a function of time t for six different rf generator output powers ranging from −20 dBm to +10 dBm, in steps of 6 dB; the amount of rf power P_{in} that enters the cavity (see figure 1) is 4.3 dB less due to losses in the directional coupler. The values in the legend between brackets indicate the rf electric field amplitude E_0 (in kV m^{-1}) in the cavity estimated from the cavity's quality factor [16].

3. Experimental evidence of collisional microwave heating

Before we proceed with the plasma model, we first experimentally investigate the effect of the rf electric field strength on the decay time of the plasma.

In a previous paper [16], we created a plasma with an initial electron temperature of 50 K, and calculated that, for the used rf electric field in the cavity (estimated to be $\lesssim$1.9 kV m^{-1} for an rf generator output power of 10 dBm), collisional microwave heating could increase the temperature by as much as $\sim 10^2$ K in the first microsecond after the plasma was created.

Here, we create a plasma with an initial electron temperature of 50 K as well, and lowered the rf power supplied to the cavity to investigate whether collisional microwave heating affects the plasma decay time.

To create a UCP, we first laser cool and trap a cloud of ^{85}Rb atoms. The trap contains 6.2×10^7 atoms, determined by fluorescence imaging, and has a Gaussian density distribution with a peak density of 1.1×10^{16} m^{-3} and rms sizes of 1.1 mm by 0.54 mm by 0.57 mm in the x-, y-, and z-direction, respectively.

Subsequently, a UCP is produced by photo-ionizing the ultracold atomic cloud with the dye laser, with on average, 420 μJ per pulse. The field-averaged electron density as a function of time t was measured for six different rf generator output powers, ranging from −20 dBm to +10 dBm; see figure 4. The density was normalized for each rf curve with respect to the density at time $t = 0$ μs, and the noisy data was smoothed with a moving average filter with a window of 500 ns to make the plasma decay trend clearer, without losing a significant amount of temporal information in the data; the $1/e$ response time (temporal resolution) of the cavity to a perturbation is, after all, 18 ns [17].

As can be seen from figure 4, the rf electric field influences the plasma lifetime; decreasing the rf power leads to a slower plasma decay. Moreover, for an rf generator output power of −8 dBm or less, the curves start to lie on top of each other and the electric field in the cavity does not seem to influence the decay time of the plasma significantly anymore; note that using this value allows us to study the UCP with MCRS non-intrusively as well.

Nevertheless, the effect of the rf electric field on the decay time of the plasma is too small to explain the discrepancy between earlier observations and the self-similar Gaussian expansion model. To fully explain the data, an additional loss mechanism is needed.

4. Analytical model for plasma expansion and wall interaction

In this section, the influence of the loss of electrons to the cavity walls is investigated. For this, a simple microscopic model was developed to calculate the flux and thus the loss of electrons to the cavity walls. This model is based on the macroscopic self-similar Gaussian expansion model, which has been described in literature before, see e.g. references [1, 35] for an in-depth treatment. Here, we first recapitulate the important steps that lead to its derivation, since we use some of the results to derive the microscopic model.

4.1. Self-similar expansion model

The self-similar Gaussian expansion model is a collisionless plasma model, with its dynamics governed by the Vlasov equation. The model assumes (1) the electrons to be in equilibrium with each other at all time

instances, (2) a Gaussian particle density distribution for both the electrons and ions, and (3) quasi-neutrality for the plasma as a whole.

The first assumption ('electron equilibrium') is justified by the small electron-to-ion mass ratio, which makes electrons very mobile on the timescales the ions move. This means that the velocity distribution of the electrons can be described by a Maxwell–Boltzmann velocity distribution

$$f_{\mathbf{v},e} = \left(\frac{m_\mathrm{e}}{2\pi k_\mathrm{B} T_\mathrm{e}(t)}\right)^{3/2} \exp\left(-\frac{m_\mathrm{e}\mathbf{v}^2}{2k_B T_\mathrm{e}(t)}\right), \tag{4}$$

at all times, with $\mathbf{v}$ the velocity of the particles.

The second assumption ('Gaussian profile') corresponds with the typical shape of a UCP produced in experiments [1]. For electrons in the cavity, the Gaussian electron density distribution n_e is given by

$$n_\mathrm{e} = \frac{N_\mathrm{e}}{(2\pi)^{3/2}\sigma^3(t)} \exp\left(-\frac{(\mathbf{r}-\mathbf{r}_0)^2}{2\sigma^2(t)}\right), \tag{5}$$

with N_e the total number of electrons in the plasma, σ the rms size of the plasma, and $\mathbf{r}_0 = \left(x_0, y_0, z_0\right)^\mathrm{T}$ the position of the center of the UCP with respect to the center of the diffraction grating chip.

Substituting the product of these distributions, which represents the electron phase space density $f_\mathrm{e} = f_{\mathbf{v},\mathrm{e}} n_\mathrm{e}$, into the electronic Vlasov equation results in the following expression for the mean-field potential φ experienced by the electrons and ions:

$$e\nabla\varphi = -\frac{k_\mathrm{B} T_\mathrm{e}(t)}{\sigma^2(t)}(\mathbf{r}-\mathbf{r}_0). \tag{6}$$

Equation (6) shows that the force $\mathbf{F}_\alpha = -q_\alpha \nabla\varphi$ acting on the particles of species α is proportional to the position with respect to the center of the plasma. For the ions, this suggests that their velocity distribution can be described by a local Maxwell–Boltzmann distribution

$$f_{\mathbf{v},i} = \left(\frac{m_\mathrm{i}}{2\pi k_\mathrm{B} T_\mathrm{i}(t)}\right)^{3/2} \exp\left(-\frac{m_\mathrm{i}(\mathbf{v}-\mathbf{u})^2}{2k_\mathrm{B} T_\mathrm{i}(t)}\right), \tag{7}$$

with $\mathbf{u} = \gamma(t)(\mathbf{r}-\mathbf{r}_0)$ the average velocity of the ions, m_i the mass of the ions, and $\gamma(t)$ a parameter describing the rate at which the plasma expands.

Substituting equations (6) and (7) into the ionic Vlasov equation, and assuming the plasma to be quasi-neutral, such that the ion density distribution $n_\mathrm{i} \approx n_\mathrm{e}$, gives a set of three differential equations for the macroscopic plasma parameters $\sigma(t)$, $\gamma(t)$, and $T_\mathrm{i}(t)$, with solutions [1]:

$$\sigma^2(t) = \sigma^2(0)\left(1 + t^2/\tau^2\right), \tag{8a}$$

$$\gamma(t) = \frac{t/\tau^2}{1 + t^2/\tau^2}, \tag{8b}$$

$$T_\mathrm{i}(t) = \frac{T_\mathrm{i}(0)}{1 + t^2/\tau^2}, \tag{8c}$$

where $\tau \equiv \sqrt{m_\mathrm{i}\sigma^2(0)/k_\mathrm{B}[T_\mathrm{e}(0) + T_\mathrm{i}(0)]}$ is the expansion time of the plasma. A fourth macroscopic plasma parameter, the electron temperature

$$T_\mathrm{e}(t) = \frac{T_\mathrm{e}(0)}{1 + t^2/\tau^2}, \tag{8d}$$

follows from the conservation of the average kinetic energy E per electron–ion pair in the plasma:

$$\frac{\mathrm{d}E}{\mathrm{d}t} = \frac{\mathrm{d}}{\mathrm{d}t}\left\{\frac{3}{2}k_\mathrm{B}[T_\mathrm{e}(t) + T_\mathrm{i}(t)] + \frac{3}{2}m_\mathrm{i}\gamma^2(t)\sigma^2(t)\right\} = 0. \tag{9}$$

Equations (8a)–(8d) give a full description of the macroscopic plasma behavior in the self-similar expansion model; they show that the phase space distributions of the electrons and ions remain Gaussian, while expanding.

4.2. Plasma-wall interaction model

However, to describe the effect of absorption of electrons by the cavity walls, we need a microscopic plasma model. To establish such a model, we first have to calculate how the positions and velocities of individual particles in the plasma change under the influence of the mean-field potential [equation (6)]. We can do

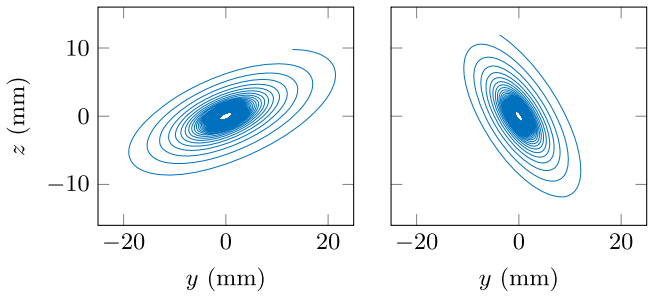

Figure 5. The trajectories of two outwards spiraling electrons with different initial positions and velocities in the *yz*-plane of the cavity.

this by substituting the solutions of the plasma rms size [equation (8a)] and the electron temperature [equation (8d)] back into equation (6). This gives an *explicit* expression for the force $\mathbf{F}_\alpha$ acting on particles of species α as a function of position and time, i.e.,

$$\mathbf{F}_\alpha = \frac{\mathrm{sgn}(q_\alpha) k_\mathrm{B} T_\mathrm{e}(0)}{\sigma^2(0)\left(1 + t^2/\tau^2\right)^2}(\mathbf{r} - \mathbf{r}_0), \tag{10}$$

with $\mathrm{sgn}(x) \equiv x/|x|$ the sign function.

The equation of motion for a single electron in the plasma then becomes

$$m_\mathrm{e}\frac{\mathrm{d}^2\mathbf{r}_\mathrm{e}}{\mathrm{d}t^2} = -\frac{k_\mathrm{B} T_\mathrm{e}(0)}{\sigma^2(0)\left(1 + t^2/\tau^2\right)^2}(\mathbf{r}_\mathrm{e} - \mathbf{r}_0), \tag{11}$$

with $\mathbf{r}_\mathrm{e}$ being the position of an electron as a function of time. Solving equation (11), and assuming that the electron temperature $T_\mathrm{e} \gg T_\mathrm{i}$ yields (see appendix A):

$$\mathbf{r}_\mathrm{e}(t) = \mathbf{r}_0 + \sqrt{1 + \frac{t^2}{\tau^2}}\left\{\frac{\mathbf{v}_{\mathrm{e},0}\tau}{\chi}\sin\left[\chi \arctan\left(\frac{t}{\tau}\right)\right] + (\mathbf{r}_{\mathrm{e},0} - \mathbf{r}_0)\cos\left[\chi \arctan\left(\frac{t}{\tau}\right)\right]\right\}, \tag{12}$$

with $\mathbf{r}_{\mathrm{e},0}$ and $\mathbf{v}_{\mathrm{e},0}$ the initial position and velocity of an electron, respectively, and $\chi^2 - 1 \equiv m_\mathrm{i}/m_\mathrm{e}$ the ion-to-electron mass ratio. The trajectories described by equation (12) represent outwardly directed spiral trajectories in a plane through the plasma. To illustrate this, we plotted the trajectories of two electrons with a different initial position $\mathbf{r}_{\mathrm{e},0}$ and initial velocity $\mathbf{v}_{\mathrm{e},0}$ as a function of time; see figure 5.

To calculate the amount of electrons lost to the cavity walls, we perform a simulation in which we follow the trajectories of $N_\mathrm{macr} \sim 10^3$ macroparticles representing a collection of electrons, with their initial positions sampled from a Gaussian electron density distribution, given by equation (5), and their initial velocities sampled from a Maxwell–Boltzmann distribution [equation (4)]. For each macroparticle k in the plasma ($k \in \{1, 2, 3, \ldots, N_\mathrm{macr}\}$), we use equation (12) to keep track of its position $\mathbf{r}_\mathrm{e}(k, t)$ in order to calculate the time $t_{\mathrm{w},k}$ at which it collides with the nearest cavity wall. Since the cavity is grounded, we assume the electrons in a macroparticle to be absorbed by the wall when this occurs; we consequently remove the macroparticle from the simulation and calculate the remaining number of electrons in the cavity (or equivalently the electron flux to the wall) as a function of time.

To compare the model with a measurement of the field-averaged electron density, we notice that the number of electrons in the cavity $N_\mathrm{e}(t) \sim \overline{n}_\mathrm{e}(t)$ for early times after the plasma is created. This is because the electric field in equation (3) is nearly constant in the region 4.8 mm $\gtrsim z \geqslant 0$ mm and $x^2 + y^2 \lesssim$ 100 mm^2 where the plasma is typically created; see figure 3.

However, for a more accurate comparison at all times during the plasma decay, we use the field map of figure 3 to determine the field-averaged electron density. The field map consists of $N_\mathrm{grid} = 273 \times 273 \times 211$ Cartesian grid points with $V_\mathrm{grid} = 0.25 \times 0.25 \times 0.25$ mm^3 the volume of a cell surrounding each grid point, and E_n the magnitude of the local electric field at the nth point ($n \in \{1, 2, 3, \ldots, N_\mathrm{grid}\}$). We calculate the field-averaged electron density by discretizing equation (3), which results in

$$\overline{n}_\mathrm{e}(t) \approx \frac{N_\mathrm{e}(0)}{N_\mathrm{macr}}\frac{\sum_{k=1}^{N_\mathrm{macr}} E^2_{f(\mathbf{r}_\mathrm{e}(k,t))} H(t_{\mathrm{w},k} - t)}{\sum_{n=1}^{N_\mathrm{grid}} E_n^2 V_\mathrm{grid}}, \tag{13}$$

with f being a function which maps the position $\mathbf{r}_\mathrm{e}(k, t)$ of the kth macroparticle at time t on the nearest gridpoint n of the electric field map, H the Heaviside step function, and $N_\mathrm{e}(0)$ the total number of electrons in the plasma at time $t = 0$.

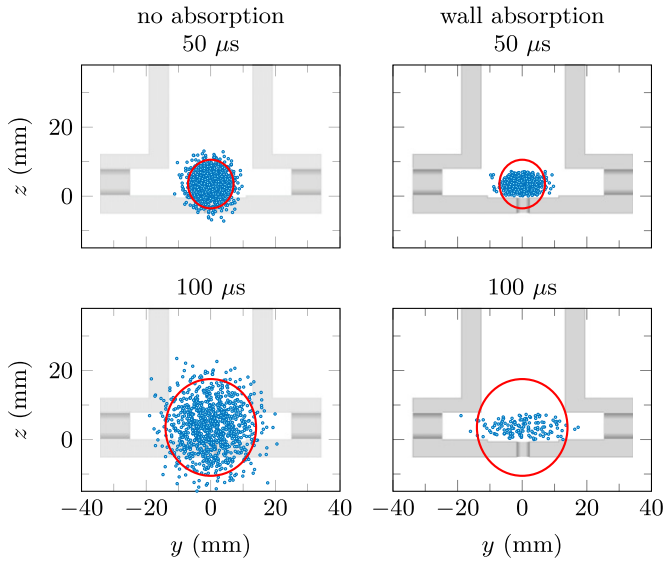

Figure 6. The particle positions in the *yz*-plane of the cavity, at time $t = 50$ μs and $t = 100$ μs for the case without wall absorption (two left figures) and the case with wall absorption (two right figures). The cavity walls are indicated in gray and the red circle drawn around the plasma, having a radius of $2\sigma(t)$, illustrates the size of the plasma according to the macroscopic model [equation (8a)].

As can be seen from equations (4), (5) and (12), our model essentially depends on four input parameters: the initial electron temperature $T_e(0)$, the initial number of electrons $N_e(0)$ in the plasma, the initial plasma rms size $\sigma(0)$, and the initial position $\mathbf{r}_0$ of the center of the plasma with respect to the diffraction grating chip.

To compare our model with the self-similar expansion model, we performed a simulation in which we track the positions of 3000 particles as a function of time, during the first 100 μs of the plasma decay, in time steps of 100 ns. We created a particle distribution with initial conditions resembling the conditions of the measurement reported in a previous paper [16]; we chose $T_e(0) = 50$ K, $N_e(0) = 5.2 \times 10^6$ electrons, $\mathbf{r}_0 = (0, 0, 3.5)^T$ mm, and, since our model assumes the plasma to have a spherical instead of ellipsoidal shape, we set $\sigma(0)$ to the geometrical mean of the rms sizes of the plasma created in reference [16], which is 410 μm.

The results of the simulation for two time steps during the plasma decay are shown in figure 6; on the left side, the particle positions in the *yz*-plane are shown for the case absorption of the particles by the cavity walls is turned off, which is equivalent to the situation described by the macroscopic self-similar expansion model, while the right side of figure 6 shows the situation where particles are absorbed by the cavity walls, as described by the microscopic model. The cavity walls are indicated in gray and a red circle with a radius of $2\sigma(t)$, containing $\sim$73% of the total amount of particles in the case without wall absorption, is drawn around the plasma to illustrate the size of the plasma according to the self-similar model [equation (8a)].

As can be noticed from figure 6, the number of electrons inside the cavity, responsible for the magnitude of the field-averaged electron density, is significantly less in the case with wall absorption than in the case without wall absorption, which could explain the faster decay in the microscopic model. In both cases, the electrons that enter the region $z < 0$ do not contribute to the field-averaged electron density, since the electric field $E = 0$ kV m^{-1}. However, a difference between the microscopic and macroscopic model originates from the spiral trajectories electrons make in the microscopic model. If such a spiral trajectory intersects with a wall, then the electron is absorbed. As a consequence, the upper part of the plasma sphere in figure 6 is empty in the case wall absorption is turned on, since these particle positions have become 'forbidden' by the microscopic model. Hence, this leads to a faster plasma decay in the microscopic model than in the macroscopic model.

4.3. Experimental verification of the model

To verify our model, we first performed MCRS measurements on UCPs with four different initial electron temperatures; see figure 7. We measured the field-averaged electron density as a function of time for decaying plasmas with an initial electron temperature set to $T_e(0) = 50$ K, 100 K, 200 K, and 500 K. The temperature was set by controlling the wavelength (photon excess energy) of the ionization laser. The

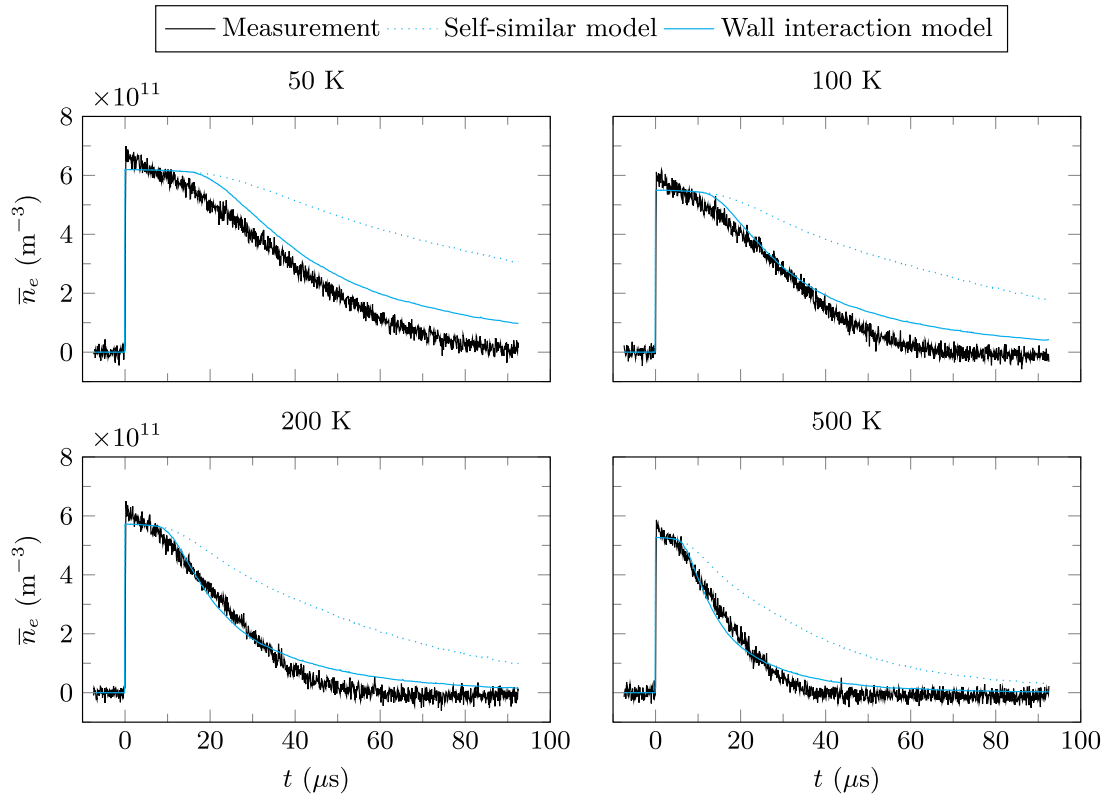

Figure 7. The field-averaged electron density $\overline{n}_e$ as a function of time t for a UCP with an initial electron temperature $T_e(0) = 50$ K, 100 K, 200 K, and 500 K.

output power of the rf generator was set to −8 dBm, such that the influence of the cavity's rf electric field on the plasma decay time is negligible, as discussed in section 3.

Subsequently, a simulation was performed and the field-averaged electron density predicted by our model was compared to the measurements.

The input parameters for our model were determined as follows. The value of the initial electron temperature $T_e(0)$ was calculated from the measured wavelength of the ionization laser, as mentioned before.

The initial number of electrons $N_e(0)$ was chosen, such that the initial measured field-averaged electron density of the 500 K curve matches the predicted one quite well. This is justified since we already showed in a previous paper [16] that we could predict $N_e(0)$ quite well (within 20% of the measured value), and since $N_e(0)$ in our model does not determine how fast the plasma decays. Using the 500 K measurement curve as a reference, gives $N_e(0) = 5.0 \times 10^6$ electrons. For the simulation of the other measurement curves, this value was scaled by the ratio of $\overline{n}_e(0)$ of the 500 K measurement curve and $\overline{n}_e(0)$ of a curve at temperature $T_e(0)$.

The initial plasma rms size was set to $\sigma(0) = 465$ μm. This value was estimated from the dimensions of the MOT and from the properties of the ionization laser beam [16]. Knowing the initial plasma rms size very accurately is, however, not important; for early times during the plasma decay, the plasma is located in a constant electric field region, and the MCRS signal therefore does not depend on the size of the plasma. For later times (when the plasma collides with the wall), the contribution of $\sigma(0)$ to the total plasma rms size $\sigma(t)$ [equation (8a)] becomes negligible. For example, when we consider the UCP with an initial electron temperature $T_e(0) = 500$ K, which starts colliding with the wall around $t = t_w \approx 6$ μs (see figure 7), then we find that the rms size $\sigma(t_w) = 1.4$ mm. However, if the initial rms size is not taken into account, then this yields $\sigma(t_w) = t_w\sqrt{k_B T_e(0)/m_i} = 1.3$ mm, a difference of only 6%, which is increasingly becoming smaller.

The initial position z_0 of the plasma above the diffraction grating chip was determined from a fluorescence image of the laser-cooled ^{85}Rb gas cloud; the image was taken with an infrared camera behind a dichroic mirror, through one of the cavity access holes, see figure 8. With the help of an accurate, in-house built computer-controlled translation stage the ionization laser beam was moved along the x- and z-direction inside the cavity, until the center of the ^{85}Rb cloud overlapped as good as possible with the center of the ionization laser beam and the measured MCRS signal is maximal; the position of the center of

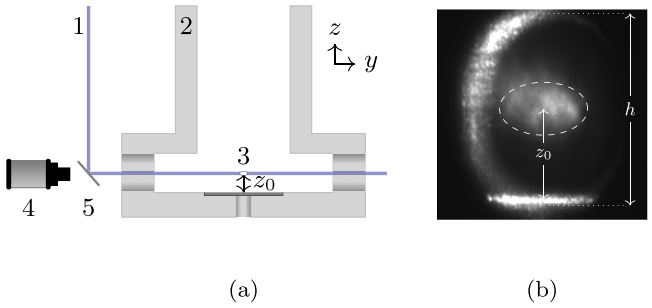

Figure 8. Determination of the position z_0 of the plasma above the diffraction grating chip. (a) With the help of a computer-controlled stage (not shown here), the ionization laser (1) is moved along the x- and z-direction in the cavity (2), until the laser overlaps best with the ^{85}Rb gas cloud (3) and the measured MCRS signal is maximal. The position of the cloud above the grating, obtained from a fluorescence image taken with an infrared camera (4) behind a dichroic mirror (5), can then be used as an estimate for z_0. (b) The actual fluorescence image used to determine the position z_0. From the known height $h = 7.5$ mm of the access hole through which the camera looks, the pixel density of the image/camera magnification was determined.

the cloud above the diffraction grating chip can then be used as an estimate for the initial position z_0 of the UCP in the cavity.

From the known height $h = 7.5$ mm of the cavity access hole, the pixel density of the fluorescence image was determined to be (127 ± 10) px/7.5 mm $\approx (17 \pm 2)$ px mm^{-1}. Multiplying the inverse of this value with the amount of pixels the atomic cloud is located above the diffraction grating chip, results in $z_0 = (3.6 \pm 0.4)$ mm. The value of $z_0 = 3.6$ mm was therefore used as an input parameter for the simulation. The positions $x_0 = y_0 = 0$ mm, since the plasma is created above the center of the diffraction grating chip.

With these input parameters, we performed a simulation of the plasma decay for each of the measured curves given in figure 7; we compared the field-averaged electron density predicted by our model ('wall interaction model') to the measurement data and $\overline{n}_e$ resulting from the self-similar expansion model.

As can be seen from figure 7, the field-averaged electron density predicted by the wall interaction model matches the measurement data quite well; there are some small deviations, but the model overall predicts the timescale at which the plasma decays, in comparison with the self-similar model, quite accurately. Moreover, it works for UCPs with different initial electron temperatures and does not require any fit parameters to do so.

4.4. Discussion of the validity of the model

Self-similarity. For the UCP with $T_e(0) = 50$ K, and for later times during the decay of each plasma, there are still some small deviations. This is, however, not surprising, since the self-similar expansion model, and therefore also the wall interaction model start to lose their validity in those cases. For $T_e(0) \lesssim 50$ K, UCP heating mechanisms, such as three-body recombination, become relevant, which cause the plasma to expand faster than solely based on the excess energy of the ionization laser's photons. In addition, the self-similar expansion model assumes the plasma to be completely neutral; in reality, many UCPs are quasi-neutral and have a small charge-imbalance due to the escape of the hot electrons right after the moment the UCP is created. In our case, we estimate the initial charge-imbalance of the UCP to be on the order of $\sim$10%, which increases for later times during the plasma decay, since we expect relatively more electrons than ions to be absorbed by the cavity walls. This might lead to a UCP that expands faster than predicted by the model at later times during the decay (see figure 7), for similar reasons as why we would expect a (completely positively charged) cloud of ions to expand faster than a neutral plasma (which is the consequence of large space-charge forces between the ions, leading to a rapid Coulomb explosion of the ion cloud).

However, in order to better predict the effect of a charge-imbalance on the plasma decay at later times during the decay, more advanced simulations should be performed that take the change of the mean-field potential due to a charge-imbalance into account.

Electron trajectories. The microscopic model we presented was based on a collisionless approach: the mean-field force acting on the electrons in the plasma lets them make spiral movements which inherently conserve the Maxwell–Boltzmann distribution [equation (4)], without the need for collisions. In reality, however, electron–electron collisions might change the directions of the electrons in the plasma, and thus their trajectories. In fact, an estimation of the electron–electron collision frequency ν_{ee} according to the

Landau–Spitzer treatment shows that, for early times during the plasma decay,

$$\nu_{ee} = \frac{1}{\sqrt{3\pi}}\omega_{p,e}\Gamma_e^{3/2} \ln \Lambda \sim 10^2 \ \mu s^{-1}. \tag{14}$$

In this equation, $\omega_{p,e} = \sqrt{n_e e^2/(m_e \epsilon_0)}$ is the electron plasma frequency, and $\ln \Lambda = \ln[(1 + b_{max}^2/b_{min}^2)^{1/2}]$ the Coulomb logarithm, with b_{min} and b_{max} the minimum and maximum impact parameter, respectively. Here, we set b_{min} to $b_{min} = e^2/\left(4\pi\epsilon_0 m_e v_{th}^2\right)$ as minimum cut-off value for the Coulomb logarithm, with $v_{th} = \sqrt{k_B T_e/m_e}$ the thermal velocity of electrons, and used the Debye length $\lambda_D = v_{th}/\omega_{p,e}$ as maximum impact parameter.

However, in the presence of an rf electric field, the Coulomb logarithm changes significantly [32]; besides the thermal motion of electrons, the ponderomotive velocity $v_{osc} = eE_0/(m_e\omega_0)$ needs to be taken into account as well, which replaces the thermal velocity v_{th} in the Coulomb logarithm by an effective velocity $v_{eff} \equiv \sqrt{v_{th}^2 + v_{osc}^2}$, and the electron plasma frequency in b_{max} by the frequency ω_0 of the rf electric field.

A calculation then shows that, for the used electric field in the cavity (estimated to be $E_0 \approx 0.2$ kV m^{-1}), the collision frequency rapidly drops to $\nu_{ee} \sim 0.1\ \mu s^{-1}$ in approximately 20 μs after the plasma is created. This time is comparable with the time it takes for the plasma to hit the wall, and the electron–electron collision time $\tau_{ee} = 1/\nu_{ee} \sim 10\ \mu$s around that moment becomes similar in size to the earlier defined expansion time $\tau \approx \sqrt{m_i\sigma^2(0)/\left[k_B T_e(0)\right]}$ of the UCP (see section 4.1). We therefore think collisions are not significant for the plasma decay, which agrees well with the measurements, but this reasoning assumes that the weakly coupled theory for the collision frequency is valid. In reality, the Landau–Spitzer theory starts to break down for $\Gamma_e \gtrsim 0.2$, which occurs for the 50 K plasma at almost the same time the collision frequency reaches $\nu_{ee} \sim 0.1\ \mu s^{-1}$. Although several expressions have been proposed recently that replace the Coulomb logarithm in equation (14) by an effective Coulomb logarithm to correct for strong coupling effects [36], to our best knowledge, none of these corrections include the effect of an rf electric field as well. In order to make a better prediction of the exact effect of collisions on our decay curves, new theory should therefore be developed that takes into account both the effects of strong coupling and an rf electric field on the Coulomb logarithm. In addition, more advanced simulations should be performed that take the change of the mean-field potential due to a charge-imbalance at later times during the plasma decay into account.

5. Collisional microwave heating

In the previous section, a model for the expansion and wall losses was developed and validated. In this section, we will extend this model to include collisional microwave heating and apply this to explain the observations made in section 3.

The collisional microwave heating rate P_{ei} for electrons in an rf electric field is given by [32]

$$P_{ei} = 2\nu_{ei}U_p, \tag{15}$$

with ν_{ei} the effective electron–ion collision frequency, which is, for $v_{osc} \lesssim v_{th}$ and apart from a factor $\sqrt{2}$, equal to the electron–electron collision frequency ν_{ee} given by equation (14), and $U_p = (eE_0)^2/(4m_e\omega_0^2)$, the ponderomotive energy of an electron in the rf electric field.

Adding this term to the right-hand side of the energy conservation equation, equation (9), as a heating source term for the electrons, and assuming the temperature of the electrons $T_e \gg T_i$, results in the following set of coupled differential equations for the macroscopic plasma parameters $\sigma(t)$, $\gamma(t)$, and $T_e(t)$:

$$\frac{\partial\sigma^2(t)}{\partial t} = 2\gamma(t)\sigma^2(t), \tag{16a}$$

$$\frac{\partial\gamma(t)}{\partial t} = \frac{k_B T_e(t)}{m_i\sigma^2(t)} - \gamma^2(t), \tag{16b}$$

$$\frac{\partial T_e(t)}{\partial t} = -2\gamma(t)T_e(t) + \frac{P_{ei}\left[E_0, T_e(t), n_e(t)\right]}{\frac{3}{2}k_B}. \tag{16c}$$

The microwave heating rate P_{ei} in equation (16c) is a function of the electric field strength E_0, the electron temperature T_e, and the electron density n_e. To couple equation (16c) to (16a), and to solve the problem, we still need to establish an additional relationship between n_e and σ. For simplicity, we ignore the spatial dependence of the electron density profile and set the electron density n_e in the microwave heating rate

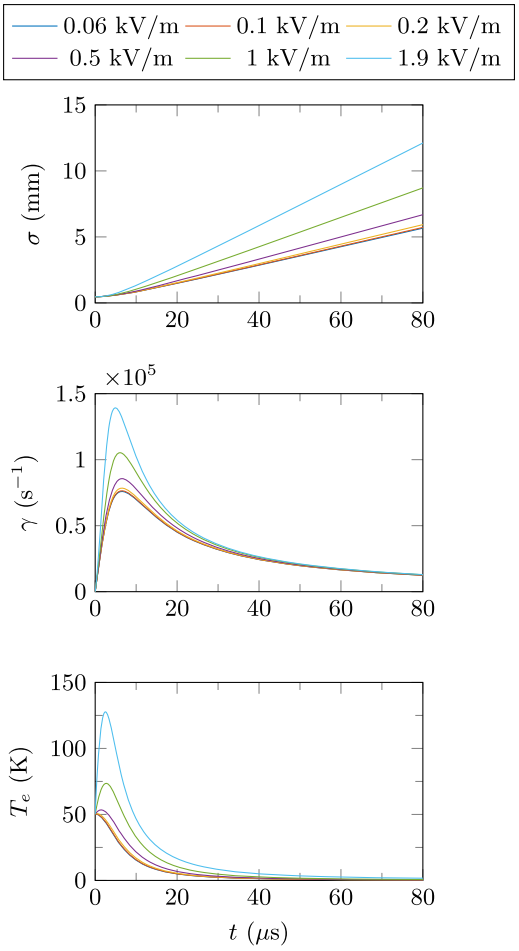

Figure 9. The macroscopic plasma parameters σ, γ, and T_e as a function of time, for different rf electric fields strengths, for initial conditions $N_e(0) = 7.4 \times 10^6$ electrons, $\sigma(0) = 4.6 \times 10^2$ μm, and $T_e(0) = 50$ K.

expression to half of the peak density of a Gaussian-shaped UCP with rms size σ, i.e.,

$$n_e(t) = \frac{\frac{1}{2}N_e(0)}{(2\pi)^{3/2}\sigma^3(t)}. \tag{16d}$$

Equations (16a)–(16d) then describe the macroscopic plasma behavior in the presence of an rf electric field, without wall absorption. The numerical solutions for the plasma parameters are illustrated in figure 9, for electric field strengths and initial conditions very similar to those for the plasma produced for the rf measurements discussed in section 3, i.e., $N_e(0) = 7.4 \times 10^6$ electrons, $\sigma(0) = 4.6 \times 10^2$ μm, and $T_e(0) = 50$ K.

As can be seen from figure 9, the electron temperature rises immediately after the UCP is created, in the presence of an rf electric field. This is because the microwave heating rate is strongest during the initial phase of the plasma expansion and then quickly drops due to an initial increase in temperature and a decreasing electron density.

To determine the plasma behavior in the case of collisional microwave heating with wall absorption, we need a microscopic plasma description again. Such a description requires a non-conservative force acting on the electrons to account for the energy increase by microwave heating, and is not easy to find. For example, simply modeling collisional microwave heating phenomenologically as an effective frictional force acting on the electrons [32] does not preserve the self-similarity of the model.

However, since the microwave heating mainly takes place during the initial phase of the plasma expansion, we assume that the heating can be taken into account by an instantaneous electron temperature increase, on top of the excess energy the electrons already obtain from the photo-ionization laser; we can then use the wall interaction model again to estimate the effect of collisional microwave heating on the plasma decay curves.

To account for the additional initial excess energy obtained from collisional microwave heating, we take the maximum electron temperature the plasma reaches for each rf electric field strength, shown in figure 9,

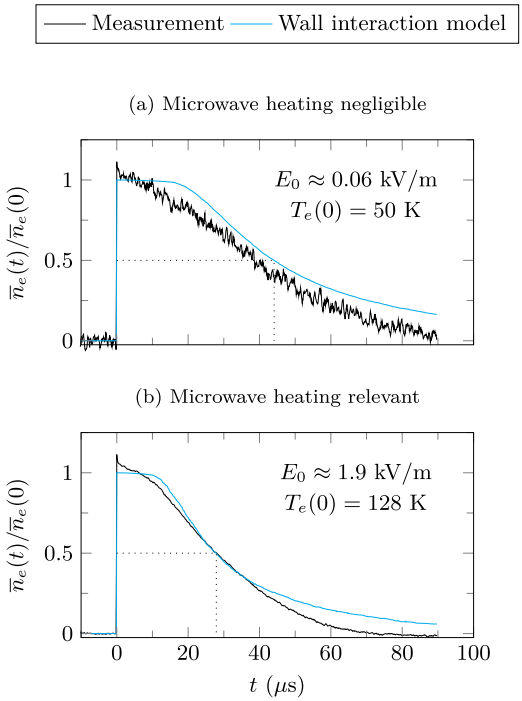

Figure 10. The measured and modeled normalized field-averaged electron density $\overline{n}_e(t)/\overline{n}_e(0)$ for a decaying UCP with $T_e(0) = 50$ K. (a) The decay in the presence of an rf electric field with size $E_0 \approx 0.06$ kV m^{-1}, where microwave heating is negligible. (b) The decay in a field with size $E_0 \approx 1.9$ kV m^{-1}, where microwave heating is relevant and leads to an increase of $T_e(0)$ to 128 K in the wall interaction model. The dotted line in both figures indicates the half-time of the modeled decay.

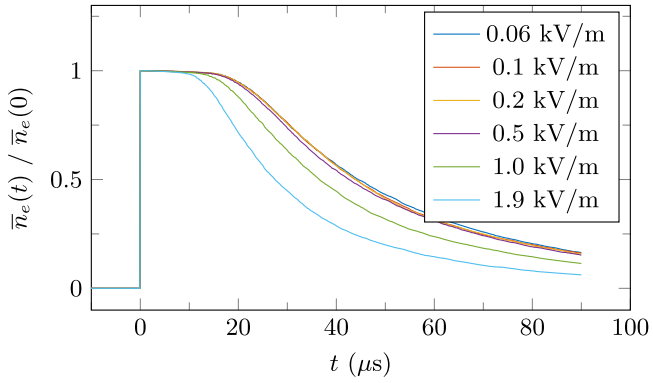

Figure 11. The modeled normalized field-averaged electron density $\overline{n}_e(t)/\overline{n}_e(0)$ as a function of time t for six different rf electric field amplitudes E_0 in the cavity. The field amplitudes correspond to the values used for the rf measurements presented in figure 4. The initial electron temperature $T_e(0)$ for each curve was set to the maximum temperature the plasma reaches in figure 9 due to collisional microwave heating.

and then perform a simulation with the wall interaction model with this temperature as initial electron temperature.

Figure 10 shows the results of the simulation for the lowest and highest rf electric field strength used in the rf measurements discussed in section 3. In figure 10(a), $E_0 \approx 0.06$ kV m^{-1}, and collisional microwave heating is negligible; the UCP indeed follows the wall interaction model with $T_e(0) = 50$ K, solely determined by the excess energy of the photo-ionization laser. In figure 10(b), however, the effect of collisional microwave heating is expected to be relevant; the electric field strength $E_0 \approx 1.9$ kV m^{-1}, which leads to a rapid temperature increase from 50 K to 128 K according to the temperature curve in figure 9. By setting $T_e(0)$ to $T_e(0) = 128$ K in the wall interaction model, and performing a simulation, we can clearly see that collisional microwave heating predicts the decay time (half-time) of the UCP quite well, see dotted line in figures 10(a) and (b).

In figure 11, the simulations for all field strengths are shown, with for each curve the initial electron temperature set to the peak value the corresponding temperature curve reaches in figure 9. The overall behavior of those curves agrees quite well with the behavior of the rf measurements presented in figure 4.

The observations of the reduced lifetime of the plasma with an increasing electric field size in the cavity, made in section 3, can therefore be explained by the existing theory of collisional microwave heating. However, to make a more realistic prediction of the effect of this heating mechanism on the plasma decay time, more advanced simulations (e.g. particle-in-cell) should be performed, preferably in combination with an improved cavity design in which the effect of the cavity wall is eliminated. This would enable us to study collisional microwave heating in a more clean way, and potentially in relationship to other competing fundamental plasma heating mechanisms of interest at low temperatures, such as three-body recombination.

6. Conclusions and outlook

We investigated the effect of collisional microwave heating and plasma–wall interactions on the decay time of a UCP measured with a resonant microwave cavity.

To study the effect of plasma–wall interactions, we developed a simple analytical microscopic model which is based on the collisionless macroscopic Gaussian self-similar expansion model. We showed that the electrons make spiral trajectories in the plasma, which lead to a faster plasma decay than predicted by the macroscopic model when taking absorption of electrons by the cavity walls into account. We validated our model with measurements of the decay of a UCP with an initial electron temperature of 50 K, 100 K, 200 K, and 500 K, and found that the model agrees well with the measurements; some small deviations, present at later times during the decay and in the 50 K measurement—which are not surprising given the analytical nature of the model—are attributed to charge-imbalance effects and collisions associated with three-body recombination, respectively.

To study the effect of collisional microwave heating, we performed measurements on the plasma decay for different rf electric field strengths in the cavity. We found that, for fields below $\sim$0.2 kV m^{-1}, the effect is negligible; this allows us to use MCRS as a non-intrusive technique for studying UCPs as well. For higher electric field strengths, there is a small, but noticeable effect on the lifetime of the plasma. By using the microscopic model again and treating the energy transferred from the microwave field to the plasma as an additional initial excess energy for the electrons, we found that the rf measurements match reasonably well with the model. This means that the effect of the electric field on the decay time of the plasma can be attributed to collisional microwave heating.

The earlier observed discrepancy of a factor of three in the decay time of the plasma between model and measurement is therefore mainly caused by plasma–wall interactions; the effect of the rf electric field on the decay time is only small.

However, more research is needed to investigate whether electron–electron collisions can alter the electron trajectories in such a way that the decay time is significantly changed. Although there are strong reasons to believe that this is not the case (the Coulomb logarithm is suppressed in the presence of an rf field when the plasma hits the nearest wall, and there is a good agreement between the measurement data and model), more advanced simulations should be performed to validate this. This should be done in combination with the development of new collision theory, since the current collision theory that corrects for strong coupling effects does not include the effect of an rf electric field on the Coulomb logarithm.

Acknowledgments

This project was financed by the Netherlands Organisation for Scientific Research (NWO) under Project No. 14651 and ASML. We would like to thank the group of Prof. Dr Riis of the University of Strathclyde (Glasgow) for supplying a diffraction grating chip for the experiments, T Secker and P Smorenburg for the fruitful discussions, and H van Doorn and E Rietman for their invaluable technical support.

Data availability statement

The data that support the findings of this study are available upon reasonable request from the authors.

Appendix A. Particle trajectories

To determine the time at which an electron in the plasma collides with a cavity wall and gets absorbed, and therefore to estimate the amount of electrons lost to the walls, we need to calculate the electron trajectories.

In this appendix, we will give a derivation for the electron trajectories, and for the ion trajectories as well. Our derivation, and thus the microscopic model presented in this paper, is based on the collisionless macroscopic self-similar expansion model; it uses the mean-field potential given by equation (6) to calculate the particle trajectories of both the electrons and ions.

As discussed in section 4.2, substitution of the solutions of the plasma rms size [equation (8a)] and electron temperature [equation (8d)] into the mean-field potential [equation (6)] leads to an explicit expression for the force acting on the particles [equation (10)] as a function of position and time. This results in the following equation of motion for the position of individual particles in the plasma

$$\left(1+t^2/\tau^2\right)^2\frac{\mathrm{d}^2\tilde{\mathbf{r}}_\alpha}{\mathrm{d}t^2}-C_\alpha\tilde{\mathbf{r}}_\alpha=0. \tag{A.1}$$

Here, $\tilde{\mathbf{r}}_\alpha\equiv\mathbf{r}_\alpha-\mathbf{r}_0$ is the position of a single particle of species α with respect to the position of the center of the plasma, C_α a constant defined as $C_\alpha\equiv\mathrm{sgn}(q_\alpha)k_\mathrm{B}T_\mathrm{e}(0)/\left[m_\alpha\sigma^2(0)\right]$, and m_α the particle mass.

Equation (A.1) represents a second-order linear ordinary differential equation with non-constant coefficients, and can be solved analytically by converting it to a constant-coefficient differential equation by using the following transformation [37]:

$$\xi\equiv\tau\ \arctan(t/\tau), \tag{A.2a}$$

$$\mathbf{w}_\alpha\equiv\tilde{\mathbf{r}}_\alpha/\sqrt{1+t^2/\tau^2}. \tag{A.2b}$$

Substitution of equation (A.2b) into (A.1) yields

$$\left(1+t^2/\tau^2\right)^{3/2}\frac{\mathrm{d}^2\tilde{\mathbf{r}}_\alpha}{\mathrm{d}t^2}-C_\alpha\mathbf{w}_\alpha=0. \tag{A.3}$$

This leaves us with calculating the second-order derivative of the particle positions $\mathrm{d}^2\tilde{\mathbf{r}}_\alpha/\mathrm{d}t^2$ in terms of $\mathbf{w}_\alpha$, which in turn can be calculated from the first-order derivative. By applying the chain rule, using the derivative of equation (A.2a), which is $\mathrm{d}\xi/\mathrm{d}t=1/\left(1+t^2/\tau^2\right)$, and by using equation (A.2b), the first-order derivative $\mathrm{d}\tilde{\mathbf{r}}_\alpha/\mathrm{d}t$ in terms of $\mathbf{w}_\alpha$ becomes

$$\begin{aligned}\frac{\mathrm{d}\tilde{\mathbf{r}}_\alpha}{\mathrm{d}t}&=\frac{\mathrm{d}\tilde{\mathbf{r}}_\alpha}{\mathrm{d}\xi}\frac{\mathrm{d}\xi}{\mathrm{d}t}\\&=\left[\frac{\mathrm{d}\mathbf{w}_\alpha}{\mathrm{d}\xi}\sqrt{1+\frac{t^2}{\tau^2}}+\mathbf{w}_\alpha\frac{\mathrm{d}}{\mathrm{d}\xi}\left(\sqrt{1+\frac{t^2}{\tau^2}}\right)\right]\frac{\mathrm{d}\xi}{\mathrm{d}t}\\&=\frac{\mathrm{d}\mathbf{w}_\alpha}{\mathrm{d}\xi}\frac{1}{\sqrt{1+t^2/\tau^2}}+\mathbf{w}_\alpha\frac{t/\tau^2}{\sqrt{1+t^2/\tau^2}}\\&=\left(\frac{\mathrm{d}\mathbf{w}_\alpha}{\mathrm{d}\xi}+\frac{t}{\tau^2}\mathbf{w}_\alpha\right)\frac{1}{\sqrt{1+t^2/\tau^2}}.\end{aligned} \tag{A.4}$$

The second-order derivative $\mathrm{d}^2\tilde{\mathbf{r}}_\alpha/\mathrm{d}t^2$ in terms of $\mathbf{w}_\alpha$ can be found in a similar way, and becomes

$$\begin{aligned}\frac{\mathrm{d}^2\tilde{\mathbf{r}}_\alpha}{\mathrm{d}t^2}&=\frac{\mathrm{d}\xi}{\mathrm{d}t}\frac{\mathrm{d}}{\mathrm{d}\xi}\left(\frac{\mathrm{d}\tilde{\mathbf{r}}_\alpha}{\mathrm{d}t}\right)\\&=\frac{\mathrm{d}\xi}{\mathrm{d}t}\left[\left(\frac{\mathrm{d}^2\mathbf{w}_\alpha}{\mathrm{d}\xi^2}+\frac{1}{\tau^2}\frac{\mathrm{d}t}{\mathrm{d}\xi}\mathbf{w}_\alpha+\frac{t}{\tau^2}\frac{\mathrm{d}\mathbf{w}_\alpha}{\mathrm{d}\xi}\right)\frac{1}{\sqrt{1+t^2/\tau^2}}-\left(\frac{\mathrm{d}\mathbf{w}_\alpha}{\mathrm{d}\xi}+\frac{t}{\tau^2}\mathbf{w}_\alpha\right)\frac{t/\tau^2}{(1+t^2/\tau^2)^{3/2}}\frac{\mathrm{d}t}{\mathrm{d}\xi}\right]\\&=\frac{1}{(1+t^2/\tau^2)^{3/2}}\left[\frac{\mathrm{d}^2\mathbf{w}_\alpha}{\mathrm{d}\xi^2}+\left(\frac{1}{\tau^2}+\frac{t^2}{\tau^4}\right)\mathbf{w}_\alpha+\frac{t}{\tau^2}\frac{\mathrm{d}\mathbf{w}_\alpha}{\mathrm{d}\xi}-\left(\frac{\mathrm{d}\mathbf{w}_\alpha}{\mathrm{d}\xi}+\frac{t}{\tau^2}\mathbf{w}_\alpha\right)\frac{t}{\tau^2}\right]\\&=\frac{1}{(1+t^2/\tau^2)^{3/2}}\left(\frac{\mathrm{d}\mathbf{w}_\alpha}{\mathrm{d}t^2}+\frac{1}{\tau^2}\mathbf{w}_\alpha\right).\end{aligned} \tag{A.5}$$

Substitution of equation (A.5) into (A.3) results in the following second-order differential equation with constant coefficients:

$$\frac{\mathrm{d}^2\mathbf{w}_\alpha}{\mathrm{d}\xi^2}+\left(\frac{1}{\tau^2}-C_\alpha\right)\mathbf{w}_\alpha=0. \tag{A.6}$$

This equation can be solved analytically by substituting the ansatz $\mathbf{w}_\alpha = \exp(-\Omega_\alpha \xi)\,\mathbf{c}$, with $\mathbf{c}$ an arbitrary vector, into the differential equation. This gives the following auxiliary equation

$$\Omega_\alpha^2 + 1/\tau^2 - C_\alpha = 0. \tag{A.7}$$

The roots Ω_α of the auxiliary equation depend on the plasma species α. For electrons, the two roots are given by

$$\begin{aligned}\Omega_\mathrm{e} &= \pm j\sqrt{\frac{1}{\tau^2} - C_\mathrm{e}} \\ &= \pm\frac{j\chi_\mathrm{e}}{\tau},\end{aligned} \tag{A.8}$$

with j the imaginary unit, and the variable χ_e defined as

$$\chi_\mathrm{e} \equiv \sqrt{1 + \frac{m_\mathrm{i}}{m_\mathrm{e}}\frac{T_\mathrm{e}(0)}{T_\mathrm{e}(0) + T_\mathrm{i}(0)}}. \tag{A.9}$$

The general solution of equation (A.6) for electrons then becomes

$$\mathbf{w}_\mathrm{e}(\xi) = \mathbf{c}_1\,\cos\left(\frac{\chi_\mathrm{e}}{\tau}\xi\right) + \mathbf{c}_2\,\sin\left(\frac{\chi_\mathrm{e}}{\tau}\xi\right), \tag{A.10}$$

with $\mathbf{c}_1$ and $\mathbf{c}_2$ two vectors depending on the initial conditions of an electron in the plasma. Rewriting equation (A.10) in terms of the electron position $\mathbf{r}_\mathrm{e}(t)$ by using equation (A.2b), yields

$$\mathbf{r}_\mathrm{e}(t) = \mathbf{r}_0 + \sqrt{1 + \frac{t^2}{\tau^2}}\left\{\mathbf{c}_1\,\sin\left[\chi_\mathrm{e}\,\arctan\left(\frac{t}{\tau}\right)\right] + \mathbf{c}_2\,\cos\left[\chi_\mathrm{e}\,\arctan\left(\frac{t}{\tau}\right)\right]\right\}. \tag{A.11}$$

The vectors $\mathbf{c}_1$ and $\mathbf{c}_2$ can be found by applying the initial conditions for the position and velocity of an electron to equation (A.11). From the initial electron position $\mathbf{r}_\mathrm{e}(t=0) = \mathbf{r}_{\mathrm{e},0}$, we find that $\mathbf{c}_2 = \mathbf{r}_{\mathrm{e},0} - \mathbf{r}_0$. The vector $\mathbf{c}_1$ can be found by first calculating the velocity $\mathbf{v}_\mathrm{e}(t)$ of an electron as a function of time, by taking the derivative of equation (A.11). This gives

$$\begin{aligned}\mathbf{v}_\mathrm{e} &\equiv \frac{\mathrm{d}\mathbf{r}_\mathrm{e}}{\mathrm{d}t} \\ &= \frac{t/\tau^2}{\sqrt{1 + t^2/\tau^2}}\left\{\mathbf{c}_1\,\sin\left[\chi_\mathrm{e}\,\arctan\left(\frac{t}{\tau}\right)\right] + (\mathbf{r}_{\mathrm{e},0} - \mathbf{r}_0)\,\cos\left[\chi_\mathrm{e}\,\arctan\left(\frac{t}{\tau}\right)\right]\right\} \\ &\quad + \frac{\chi_\mathrm{e}\tau}{t^2 + \tau^2}\sqrt{1 + \frac{t^2}{\tau^2}}\left\{\mathbf{c}_1\,\cos\left[\chi_\mathrm{e}\,\arctan\left(\frac{t}{\tau}\right)\right] - (\mathbf{r}_{\mathrm{e},0} - \mathbf{r}_0)\,\sin\left[\chi_\mathrm{e}\,\arctan\left(\frac{t}{\tau}\right)\right]\right\}.\end{aligned} \tag{A.12}$$

By using the initial condition for the electron velocity $\mathbf{v}_\mathrm{e}(t=0) = \mathbf{v}_{\mathrm{e},0}$, we find that $\mathbf{c}_1 = \mathbf{v}_{\mathrm{e},0}\tau/\chi_\mathrm{e}$.

The full solution of a trajectory of an electron in the plasma is then described by

$$\mathbf{r}_\mathrm{e}(t) = \mathbf{r}_0 + \sqrt{1 + \frac{t^2}{\tau^2}}\left\{\frac{\mathbf{v}_{\mathrm{e},0}\tau}{\chi_\mathrm{e}}\,\sin\left[\chi_\mathrm{e}\,\arctan\left(\frac{t}{\tau}\right)\right] + (\mathbf{r}_{\mathrm{e},0} - \mathbf{r}_0)\,\cos\left[\chi_\mathrm{e}\,\arctan\left(\frac{t}{\tau}\right)\right]\right\}. \tag{A.13}$$

This represents a spiral trajectory in a plane through the plasma.

The ion trajectories can be found in a similar way. The roots of the auxiliary equation for ions are given by

$$\begin{aligned}\Omega_\mathrm{i} &= \pm j\sqrt{\frac{1}{\tau^2} - C_\mathrm{i}} \\ &= \pm\frac{j\chi_\mathrm{i}}{\tau},\end{aligned} \tag{A.14}$$

with the variable χ_i defined as

$$\chi_\mathrm{i} \equiv \sqrt{\frac{T_\mathrm{i}(0)}{T_\mathrm{e}(0) + T_\mathrm{i}(0)}}. \tag{A.15}$$

The remaining steps for finding the trajectories are completely analogous to those discussed above for finding the electron trajectories; the steps result in almost the same solution for the ion trajectories, with the only exception that χ_e in equation (A.13) is replaced by χ_i. As a consequence, the ions will move in spiral trajectories as well, but on a much larger time scale in comparison with the electrons; the latter is caused by the much heavier mass and lower initial temperature of the ions in a UCP.

ORCID iDs

M A W van Ninhuijs https://orcid.org/0000-0002-0577-3403
J Beckers https://orcid.org/0000-0001-6116-7013
O J Luiten https://orcid.org/0000-0003-2048-4455

References

[1] Killian T C, Pattard T, Pohl T and Rost J M 2007 *Phys. Rep.* **449** 77
[2] Killian T C, Kulin S, Bergeson S D, Orozco L A, Orzel C and Rolston S L 1999 *Phys. Rev. Lett.* **83** 4776
[3] Lyon M and Rolston S L 2016 *Rep. Prog. Phys.* **80** 017001
[4] Hayashi Y and Tachibana K 1994 *Japan. J. Appl. Phys.* **33** L804
[5] Chu J H and Lin I 1994 *Phys. Rev. Lett.* **72** 4009
[6] Thomas H, Morfill G E, Demmel V, Goree J, Feuerbacher B and Möhlmann D 1994 *Phys. Rev. Lett.* **73** 652
[7] Van Horn H M 1991 *Science* **252** 384
[8] Ichimaru S 1982 *Rev. Mod. Phys.* **54** 1017
[9] Mansbach P and Keck J 1969 *Phys. Rev.* **181** 275
[10] Kuzmin S G and O'Neil T M 2002 *Phys. Rev. Lett.* **88** 065003
[11] Murillo M S 2001 *Phys. Rev. Lett.* **87** 115003
[12] Langin T K, Gorman G M and Killian T C 2019 *Science* **363** 61
[13] Cummings E A, Daily J E, Durfee D S and Bergeson S D 2005 *Phys. Rev. Lett.* **95** 235001
[14] Simien C E, Chen Y C, Gupta P, Laha S, Martinez Y N, Mickelson P G, Nagel S B and Killian T C 2004 *Phys. Rev. Lett.* **92** 143001
[15] Killian T C, Ashoka V S, Gupta P, Laha S, Nagel S B, Simien C E, Kulin S, Rolston S L and Bergeson S D 2003 *J. Phys. A: Math. Gen.* **36** 6077
[16] Van Ninhuijs M A W, Daamen K A, Franssen J G H, Conway J, Platier B, Beckers J and Luiten O J 2019 *Phys. Rev.* A **100** 061801
[17] Van Ninhuijs M A W, Daamen K A, Beckers J and Luiten O J 2021 *Rev. Sci. Instrum.* **92** 013506
[18] Nshii C C *et al* 2013 *Nat. Nanotechnol.* **8** 321
[19] McGilligan J P, Griffin P F, Riis E and Arnold A S 2016 *J. Opt. Soc. Am.* B **33** 1271
[20] Brown S C and Rose D J 1952 *J. Appl. Phys.* **23** 711
[21] Rose D J and Brown S C 1952 *J. Appl. Phys.* **23** 719
[22] Rose D J and Brown S C 1952 *J. Appl. Phys.* **23** 1028
[23] Haverlag M, Kroesen G M W, Bisschops T H J and de Hoog F J 1991 *Plasma Chem. Plasma Process.* **11** 357
[24] Stoffels E, Stoffels W W, Vender D, Kando M, Kroesen G M W and de Hoog F J 1995 *Phys. Rev.* E **51** 2425
[25] Vender D, Stoffels W W, Stoffels E, Kroesen G M W and de Hoog F J 1995 *Phys. Rev.* E **51** 2436
[26] Beckers J, Stoffels W and Kroesen G M W 2009 *J. Phys. D: Appl. Phys.* **42** 155206
[27] Beckers J, Van de Wetering F M J H, Platier B, Van Ninhuijs M A W, Brussaard G J H, Banine V Y and Luiten O J 2018 *J. Phys. D: Appl. Phys.* **52** 034004
[28] Van der Schans M, Platier B, Koelman P, Van de Wetering F, Van Dijk J, Beckers J, Nijdam S and IJzerman W 2019 *Plasma Sources Sci. Technol.* **28** 035020
[29] Platier B, Staps T J A, Van der Schans M, IJzerman W L and Beckers J 2019 *Appl. Phys. Lett.* **115** 254103
[30] Platier B, Staps T J A, Hak C C J M, Beckers J and IJzerman W L 2020 *Plasma Sources Sci. Technol.* **29** 045024
[31] Kulin S, Killian T C, Bergeson S D and Rolston S L 2000 *Phys. Rev. Lett.* **85** 318
[32] Smorenburg P W, Kamp L P J and Luiten O J 2012 *Phys. Rev.* A **85** 063413
[33] Pozar D M 2011 *Microwave Engineering* 4th edn (New York: Wiley)
[34] CST Microwave Studio (https://cst.com/products/cstmws) retrieved August 2020
[35] Mendonça J T and Terças H 2013 *Physics of Ultra-cold Matter: Atomic Clouds, Bose-Einstein Condensates and Rydberg Plasmas* (*Springer Series on Atomic, Optical, and Plasma Physics* vol 70) (Berlin: Springer)
[36] Bannasch G, Castro J, McQuillen P, Pohl T and Killian T C 2012 *Phys. Rev. Lett.* **109** 185008
[37] Polyanin A D and Zaitsev V F 2018 *Handbook of Ordinary Differential Equations: Exact Solutions, Methods, and Problems* 1st edn (Boca Raton, FL: CRC Press)